Nano Research
2022, 15(3): 1861–1867

ISSN 1998-0124 CN 11-5974/O4
https://doi.org/10.1007/s12274-021-3786-0

Research Article

Atomically isolated Pd sites within Pd-S nanocrystals enable trifunctional catalysis for direct, electrocatalytic and photocatalytic syntheses of H_2O_2

Tang Yang[1,§], Chengyong Yang[1,2,§], Jiabo Le[1], Zhiyong Yu[2], Lingzheng Bu[1] (✉), Leigang Li[2], Shuxing Bai[2], Qi Shao[2], Zhiwei Hu[3], Chih-Wen Pao[4], Jun Cheng[1] (✉), Yonggang Feng[2], and Xiaoqing Huang[1] (✉)

[1] *State Key Laboratory of Physical Chemistry of Solid Surfaces, College of Chemistry and Chemical Engineering, Xiamen University, Xiamen 361005, China*
[2] *College of Chemistry, Chemical Engineering and Materials Science, Soochow University, Suzhou 215123, China*
[3] *Max-Planck-Institute for Chemical Physics of Solids, Nöthnitzer Street 40, Dresden 01187, Germany*
[4] *"National Synchrotron Radiation Research Center", Hsinchu 30076, Taiwan, China*
[§] *Tang Yang and Chengyong Yang contributed equally to this work.*

Received: 4 June 2021 / **Revised:** 26 July 2021 / **Accepted:** 1 August 2021

ABSTRACT

Although high-efficiency production of hydrogen peroxide (H_2O_2) can be realized separately by means of direct, electrochemical, and photocatalytic synthesis, developing versatile catalysts is particularly challenging yet desirable. Herein, for the first time we reported that palladium-sulphur nanocrystals (Pd-S NCs) can be adopted as robust and universal catalysts, which can realize the efficient O_2 conversion by three methods. As a result, Pd-S NCs exhibit an excellent selectivity (89.5%) to H_2O_2 with high productivity (133.6 $mol \cdot kg_{cat}^{-1} \cdot h^{-1}$) in the direct synthesis, along with the significantly enhanced H_2O_2 production activity and stability via electrocatalytic and photocatalytic syntheses. It is demonstrated that the isolated Pd sites can enhance the adsorption of O_2 and inhibit its O–O bond dissociation, improving H_2O_2 selectivity and reducing H_2O_2 degradation. Further study confirms that the difference in surface atom composition and arrangement is the key factor for different ORR mechanisms on Pd NCs and Pd-S NCs.

KEYWORDS

Pd-S, universality, direct synthesis of H_2O_2, oxygen reduction, photocatalysis

1 Introduction

Hydrogen peroxide (H_2O_2), as an environmentally benign and atom-economical oxidizing agent, is widely used in chemical synthesis, environmental protection, agriculture and many other fields [1–6]. Currently, the industrial method of large-scale production of H_2O_2 is the anthraquinone process, which involves the sequential hydrogenation and oxidation of anthraquinone molecules [7]. Despite that this technology is mature, it still faces formidable practical sustainability challenges, such as environmental pollution, high energy consumption, industrial waste handling as well as the high cost of capital and operating [8–11]. Thus, developing a highly efficient and economic method to replace the traditional anthraquinone process has important implications for addressing environmental issues and energy depletion.

The ever-increasing demand for H_2O_2 has stimulated substantial efforts to develop the most promising catalysts for H_2O_2 synthesis [12–16]. Up to now, the direct synthesis of H_2O_2 (DSHP) [17–21], $2e^-$-electrochemical oxygen reduction reaction (ORR) [22] and photocatalytic H_2O_2 production [23–27] represent three most attractive approaches for producing H_2O_2 with the merits of environmentally friendliness, high efficiency and high safety [28–31]. However, the O–O bond dissociation can readily occur as a side reaction simultaneously during the DSHP, ORR [32–35] or photocatalytic H_2O_2 production that severely degrades the catalytic selectivity [36–40]. The conventional methods of tackling this issue are to increase the number of isolated metal sites on catalyst surface by forming alloy [41], preparing single-atom catalysts [42–44], etc. For example, Hutchings et al. had synthesized a range of Pd-Sn alloy nanoparticles by an appropriate oxidation-reduction-oxidation heat treatment process, which exhibit very high selectivity (> 95%) for H_2O_2 production in the DSHP [37]. Choi et al. synthesized atomically dispersed Pt catalyst on zeolite-templated carbon (ZTC) containing an extra-large amount of sulfur via a simple wet-impregnation method, which selectively catalyzes a $2e^-$-ORR pathway for producing H_2O_2 [42]. Hirai et al. found Au-Ag alloy could produce H_2O_2 by UV irradiation [41]. Although high selectivity of H_2O_2 production has been achieved via different methods, there are no versatile catalysts that could simultaneously achieve high productivity in the direct H_2O_2 synthesis, electrocatalytic and photocatalytic H_2O_2 synthesis. It is highly desirable to design universal catalysts to realize high yield of H_2O_2 production simultaneously through direct,

Address correspondence to Lingzheng Bu, lzbu@xmu.edu.cn; Jun Cheng, chengjun@xmu.edu.cn; Xiaoqing Huang, hxq006@xmu.edu.cn

electrocatalytic and photocatalytic H_2O_2 synthesis, which could largely profit the catalyst utilization efficiency.

Herein, we demonstrated that unique Pd-S nanocrystals (NCs) can be adopted as a high activity, selectivity and universal catalyst for the synthesis of H_2O_2. Compared with Pd NCs, Pd-S NCs can achieve an excellent H_2O_2 production rate of 133.6 mol·kg_{cat}^{-1}·h^{-1} with 89.5% selectivity of H_2O_2 in the DSHP. The Pd-S NCs also show promising activity in both electrocatalytic and photocatalytic H_2O_2 synthesis. It is found that, the electronic transition between Pd and S results in high electron density at Pd sites, benefiting the adsorption of O_2, while the improved selectivity is attributed to the presence of isolated active Pd atoms, which can inhibit the dissociation of O–O bond. In addition, Pd-S NCs can also maintain satisfactory stability with small activity decay in the H_2O_2 synthesis.

2 Experimental

2.1 Material preparation

Including palladium(II) bromide ($PdBr_2$), sulfocarbamide (CH_5N_3S), L-ascorbic acid ($C_6H_8O_6$, AA), and oleylamine ($C_{18}H_{37}N$, OAm), ethanol (CH_3CH_2OH, analytical reagent, ≥ 99.8%), methanol (CH_3OH, analytical reagent, ≥ 99.5%), sulphuric acid (H_2SO_4, analytical reagent, 95%–98%), all the materials and solvents used in this study were described in our previous works [45, 46]. All the chemicals were used as received without further purification.

2.2 Preparation of Pd-S NCs

For typical synthesis of Pd-S NCs, 6.1 mg $PdBr_2$, 1.1 mg sulfocarbamide, 36 mg AA, and 5 mL OAm were added into a glass vial. This mixture was sonicated for 0.5 h, then heated to 160 °C and reacted for 5 h. After cooling to 20 °C, the products were washed for twice with a cyclohexane/ethanol mixture (v/v = 1/9) and collected by centrifugation.

2.3 Characterizations

Power X-ray diffraction (PXRD) patterns were collected using an X`Pert-Pro X-ray powder diffractometer equipped with a Cu radiation source (λ = 0.15406 nm). The morphology and size of these NCs were determined by transmission electron microscopy (TEM, Hitachi, HT7700) at 120 kV. High-resolution TEM (HRTEM), TEM energy dispersive X-ray spectroscopy (TEM-EDS), high-angle annular dark-field scanning TEM (HAADF-STEM), and HAADF-STEM-EDS elemental mappings were conducted on a FEI Tecnai F20 TEM at an accelerating voltage of 200 kV. Low-resolution EDS was performed on a scanning electron microscope (SEM-EDS, Hitachi, S-4700). All the X-ray photoelectron spectroscopy (XPS) spectra were collected by XPS (Thermo Scientific, ESCALAB 250 XI). The concentration of catalyst was analyzed by the inductively coupled plasma atomic emission spectroscopy (ICP-AES, 710-ES, Varian). All these characterization techniques used in this work were described in our previous works [47, 48]. The X-ray absorption spectroscopy (XAS) data were collected at the TPS-44A beamline of the "National Synchrotron Radiation Research Center" (NSRRC, Hsinchu, Taiwan, China) using a Si (111) quick-scanning monochromator. All the XAS data were processed according to standard procedures using the Demeter program package (Version 0.9.24). Diffuse reflectance infrared Fourier transform spectroscopy (DRIFTS) experiments were similar to the previous study [49]. The background spectrum was acquired after flowing 0.1 MPa Ar for 0.5 h. 0.1 MPa CO and Ar were then allowed to flow into the cell at room temperature for 1.0 and 0.5 h, respectively.

2.4 Catalytic tests

H_2O_2 synthesis by DSHP: For the DSHP, 5 mg catalyst and 10 mL solvent (MeOH and H_2O (v/v = 7/3)) were added into an autoclave. The autoclave was then purged for three times with O_2 (0.2 MPa) before filling with O_2 to a pressure of 0.4 MPa at room temperature. This was followed by the addition of 5% H_2/N_2 (3.6 MPa). Then, in an ice bath, the reaction was carried out at 800 rpm for 0.5 h. The productivity of H_2O_2 was confirmed by the titration volume of acidified $Ce(SO_4)_2$ (0.01 M), and the developer was ferroin indicator. Gas analysis was carried out with GDX-502 column gas chromatography (GC shiweipx-7806) equipped with a thermal conductivity detector. The conversion rate of H_2 was calculated by the change of H_2 before and after the reaction by gas analysis. H_2O_2 degradation and hydrogenation experiments were carried out in a similar manner to that of the H_2O_2 synthesis. The standard reaction conditions adopted for H_2O_2 degradation were as follows: 5 mg catalyst, 10 mL solvent (7 mL MeOH, 1.97 mL H_2O and 1.03 mL H_2O_2 (30 %)), 3.6 MPa 5% H_2/N_2, 0 °C, 800 rpm, 0.5 h.

The selectivity of DSHP and the H_2 conversion were calculated based on the following formulas

$$\text{Conversion}\,(H_2) = \frac{n(H_2O_2)+n(H_2O)}{n(H_2)_{\text{feed}}} = \frac{n(H_2)_{\text{reacted}}}{n(H_2)_{\text{feed}}}$$

$$\text{Selectivity}\,(H_2O_2) = \frac{n(H_2O_2)}{n(H_2O)+n(H_2O_2)} = \frac{n(H_2O_2)}{n(H_2)_{\text{reacted}}}$$

H_2O_2 synthesis by ORR: For ORR, the rotating ring-disk electrode (RRDE) setup was used to perform the electrochemical measurements. The electrode was rotated using a Pine Instrument Company (GroveCity, PA) FMSRX rotator and MSRX speed controller. The electrolyte was 0.05 M H_2SO_4 and the reference electrode was saturated calomel electrode (SCE). A carbon rod was used as the counter electrode. The reference electrode was calibrated against and converted to reversible hydrogen electrode (RHE). The RRDE with a glassy carbon disk (geometric area 0.196 cm^2) and Pt ring was used as the working electrode. The catalyst ink (contain carbon, 1 mg·mL^{-1}, 5 μL, 20.2% mass loading amount of Pd) was dropped on the glassy carbon disk and dried at room temperature. ORR measurement was carried out in aqueous solution of 0.05 M H_2SO_4 purged with O_2. The scan rate was 10 mV·s^{-1} and rotation rate was 1,600 rpm for the ORR measurement. The ring currents were recorded by fixing the ring potential at 1.2 V (vs. RHE) to detect the H_2O_2. The durability tests were performed at room temperature in O_2-saturated aqueous solution of 0.05 M H_2SO_4 by applying the cyclic potential sweeps at a sweep rate of 100 mV·s^{-1} for 5,000 cycles. Selectivity of the catalysts toward H_2O_2 formation was calculated using the following Eq. (1)

$$H_2O_2\% = 200 \times (I_R/N) / (I_R/N - I_D) \quad (1)$$

The number of transferred electrons (n) at the disk electrode during oxygen reduction process was calculated using the following Eq. (2)

$$n = 4 \times |I_D| / (I_R/N - I_D) \quad (2)$$

where I_D is the disk current, I_R is the ring current and N is the collection efficiency. The value of N was experimentally determined to be 0.29 by using a standard ferricyanide system.

H_2O_2 synthesis by photocatalysis: 10 mg catalyst was dissolved in 20 mL solvent (1 mL EtOH and 19 mL H_2O). Then bubbling with high purity O_2 for 30 min to keep the O_2 balance in the entire

system. Finally, visible light irradiation was applied to the system for 2 h. To obtain the calibration curve, the H_2O_2 solution of known concentration was added to the $Ce(SO_4)_2$ solution and measured using a Techcomp 2600 UV Spectrometer at 316 nm. Based on the linear relationship between signal intensity and Ce^{4+} concentration, the H_2O_2 concentrations of different samples can be obtained.

2.5 Computational details

All the density functional theory (DFT) calculations were carried out by Vienna *ab-initio* simulation package (VASP), and Perdew–Burke–Ernzerhof (PBE) functional [50] was employed to describe the exchange-correlation effect. The plane waves were constructed using projector augmented-wave (PAW) potentials with an energy cutoff of 450 eV, and the convergence criteria for the geometry optimization was the maximum force of the unconstrained atoms less than 0.05 eV·Å^{-1}.

The lattice parameters of bulk Pd and Pd_4S were optimized initially, and then the Pd (111) and S-terminated Pd_4S (110) surfaces were chosen for this study because they are most stable in thermodynamics. As shown in Fig. S11(a) in the ESM and Fig. 1(b), the Pd (111) surface was modeled by a 3 × 3 supercell slab with 3 atomic layers. The vacuum space between the slabs is 15 Å, and a 4 × 4 × 1 *k*-point is employed. For the S-terminated Pd_4S (110) surface, it is represented by a 2 × 1 supercell with 4 Pd-S layers, as seen in Figs. S11(c) and S11(d) in the ESM. The vacuum space between the slabs is also set to 15 Å, and a 2 × 3 × 1 *k*-point is employed. To avoid the dipole interaction with periodic images, a dipole correction was set in the surface normal direction. During the structural optimization of the adsorbates, the bottom two layers of the slabs were fixed, and for the frequency calculation, only the adsorbates were relaxed. To obtain the activation energies of the reaction steps, a bond length approach and the climbing image nudged elastic band (CI-NEB) calculation were used to search for the transition states.

The Gibbs reaction free energy (ΔG) was calculated with $\Delta G = \Delta E + \Delta ZPE - T\Delta S$, where ΔE, ΔZPE and $T\Delta S$ denote for the difference in total energy, zero-point energy and entropy, respectively. The solvation effect on the ORR reaction is complicated and still not clear. For simplification, we fully ignored the role of solvation in this study because we think it does not affect the qualitative comparison between Pd (111) and Pd_4S (110) for O–O bond dissociation.

3 Results and discussion

The Pd-S NCs were prepared by a simple wet-chemical method (details in the Experimental section). Figure 1(a) shows the TEM image of Pd-S NCs. It can be seen that the Pd-S NCs are highly uniform and monodisperse with an average diameter of 10.8 nm (Fig. S1(a) in the ESM). The composition of the Pd-S NCs was determined to be Pd/S = 66.5/33.5 by SEM-EDS spectrum (Fig. S1(b) in the ESM), being consistent with the ICP-AES result. PXRD analysis was conducted to identify the crystalline structure of Pd-S NCs. As seen in Fig. 1(b), the PXRD pattern of Pd-S NCs reveals a tetragonal phase, where the diffraction peaks at 23.7°, 35.1°, 39.5°, 40.8°, 51.6° and 80.5° can be mainly indexed to (101), (200), (210), (112), (212) and (214) facets of Pd_4S phase, respectively (JCPDS file, No. 10-0335).

The Pd-S NCs crystallize in a tetragonal symmetry with the space group of $P\bar{4}21c$ (114). The projected unit cell is composed

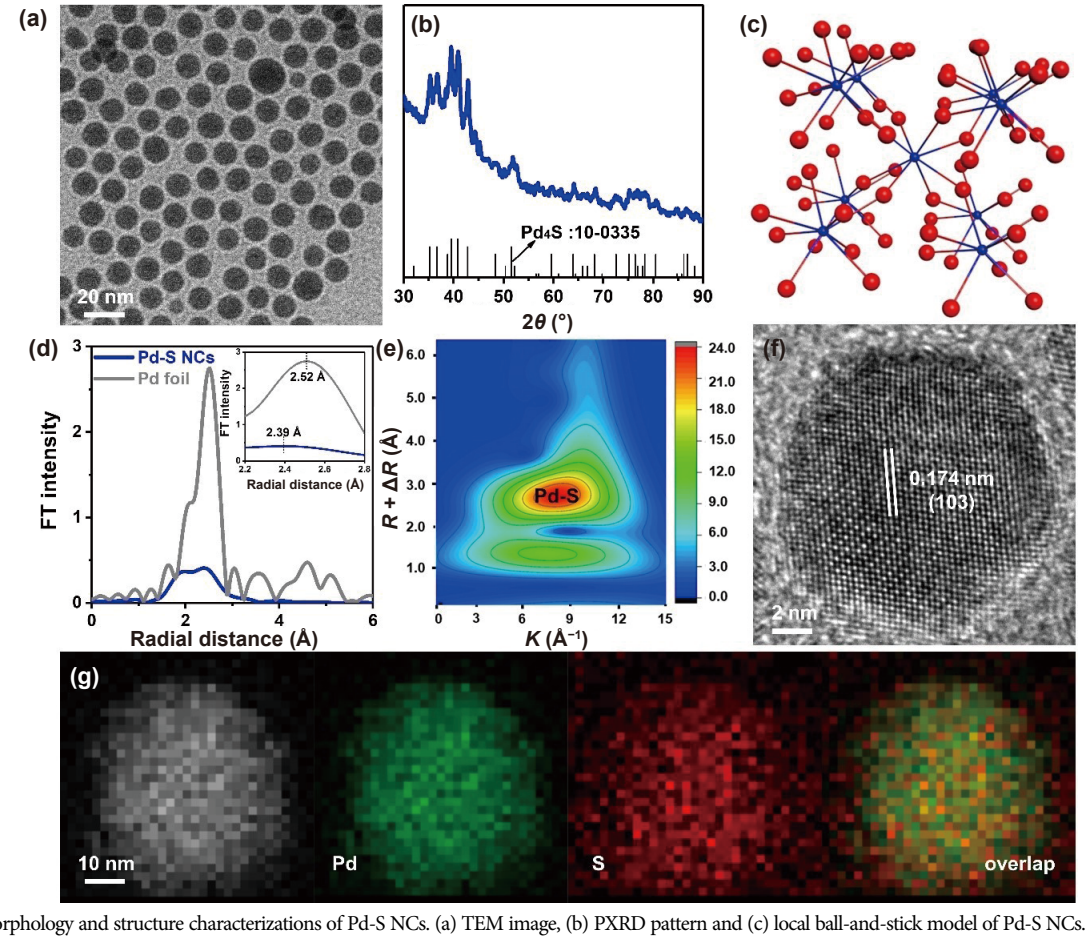

Figure 1 Morphology and structure characterizations of Pd-S NCs. (a) TEM image, (b) PXRD pattern and (c) local ball-and-stick model of Pd-S NCs. Pd: red, and S: blue. (d) Fourier transforms for EXAFS spectra of Pd K-edge. The inset in (d) is the enlarged picture. (e) Wavelet transforms for EXAFS spectra, (f) HRTEM image, and (g) HAADF-STEM image and elemental mapping of the Pd-S NCs.

of two non-equivalent Pd–S metallic bonds (Fig. 1(c)). The XAS technique was adopted to reveal the local environment and chemical bonding of Pd-S NCs. The Fourier transformation of the Pd K-edge extended X-ray absorption fine structure (EXAFS) of Pd-S NCs is shown in Fig. 1(d) and compared with that of Pd foil. The peak at 2.52 Å for the Pd foil can be attributed to Pd–Pd bond. A clear shift of the first shell bond length from 2.52 to 2.39 Å suggests that there is no clear Pd–Pd bond feature in Pd-S NCs, confirming the presence of isolated Pd atoms in the Pd-S NCs. Wavelet transform (WT) at the Pd K-edge EXAFS analysis further confirms the isolated state of Pd atoms (Fig. 1(e)), only a maximum intensity at approximately 8.7 $Å^{-1}$ attributes to the S–Pd bond. HRTEM further confirmed the crystalline properties of Pd-S NCs (Fig. 1(f)), in which a crystal plane spacing of 0.174 nm was clearly observed assigned to the (103) plane of Pd_4S phase. The HAADF-STEM image and corresponding elemental mappings demonstrate that Pd and S are uniformly distributed in the whole NCs (Fig. 1(g)).

To highlight the distinct structure of Pd-S NCs for catalysis, DSHP was firstly carried out. Both the Pd-S NCs and Pd NCs loaded on TiO_2 were used as catalysts (Fig. S2 in the ESM). The Pd NCs exhibit relatively poor activities for the direct H_2O_2 production, where they exhibit low activities of only 35 $mol \cdot kg_{cat}^{-1} \cdot h^{-1}$ (Fig. 2(a)).

In contrast, the Pd-S NCs reach impressive activity of 133.6 $mol \cdot kg_{cat}^{-1} \cdot h^{-1}$, indicating that the distinct structure significantly improves the activity of Pd for the direct H_2O_2 production. We also compared the H_2O_2 selectivity and H_2O_2 degradation, where the Pd-S NCs exhibit the highest selectivity (89.5%) and the lowest degradation activity (22 $mol \cdot kg_{cat}^{-1} \cdot h^{-1}$) (Figs. 2(b) and 2(c)). The rate of H_2O_2 hydrogenation on different catalysts was also investigated, where the Pd-S NCs exhibit the lowest activity for H_2O_2 hydrogenation (Fig. 2(d)). The turn over frequency (TOF) for Pd-S NCs was calculated to be 15,891 h^{-1} by normalizing the surface atom number via CO stripping (Fig. S3 in the ESM), which is 3.6 times higher than that of Pd NCs (4,395 h^{-1}). It is worth noting that the H_2O_2 selectivity and productivity of Pd-S NCs are higher than many reported materials (Table S1 in the ESM). We also investigated the recyclability of Pd-S NCs under the same condition, where the catalytic performance did not show obvious activity loss in the four sequential cycles after the initial run (Fig. S4 in the ESM). The additional characterizations of Pd-S NCs also showed the well-maintained morphology (Fig. S5(a) in the ESM) with only slight leaching of Pd (Fig. S5(b) in the ESM) after DSHP catalysis.

We then investigated the performance of Pd-S NCs towards electrocatalytic H_2O_2 synthesis. The $2e^-$-ORR performance was evaluated with RRDE method at 1,600 rpm in O_2-saturated 0.05 M H_2SO_4. Both Pd-S NCs and Pd NCs were separately supported on commercial carbon (Fig. S6 in the ESM). Figure 3(a) shows the electrochemical result in 0.05 M H_2SO_4. The oxygen reduction currents were measured on a disk electrode and the H_2O_2 oxidation currents were measured on a Pt ring electrode. As shown in Fig. 3(a), Pd-S NCs reveals an onset potential of 0.72 V vs. RHE, close to the thermodynamic potential of H_2O_2 production ($U_0^{O2/H2O2}$ = 0.7 V vs. RHE), and a high current density with respect to the Pd NCs, indicating that Pd-S NCs exhibit higher activity for H_2O_2 production. The H_2O_2 selectivity can be calculated by RRDE experiments. As shown in Fig. 3(b), the H_2O_2 selectivity of Pd-S NCs is more than 90% at a potential between 0.2 and 0.45 V (vs. RHE), while the Pd NCs exhibit a H_2O_2 production selectivity of lower than 20%. Moreover, the number of transferred electrons (n) for Pd-S NCs was calculated to be around 2.2 from 0.2 to 0.45 V (vs. RHE), indicating a dominant $2e^-$-O_2 reduction pathway, while Pd NCs catalyzes the ORR predominately through a $4e^-$ pathway (n = 3.7, Fig. 3(c)). All the results above have clearly revealed that the Pd-S NCs is also very promising towards electrocatalytic H_2O_2 synthesis (Table S2 in the ESM).

The potential of producing H_2O_2 during the $2e^-$-ORR process was tested in an electrochemical H-cell. Figure S7 in the ESM shows the accumulated amount of H_2O_2, normalized by the reaction time at the different applied potentials from 0.2 to 0.4 V in O_2-saturated 0.05 M H_2SO_4. It can be observed that the H_2O_2 production rate increases with the negative shift of potential in the investigated potential range. The concentration of H_2O_2 increases linearly as a function of reaction time, indicating the stable and continuous H_2O_2 production. Remarkably, the production rate of H_2O_2 is up to 12.5 $mmol \cdot L^{-1}$ at 0.2 V (vs. RHE). To evaluate their ORR durability, we measured ORR polarization curves before and after durability test for 5,000 cycles, where the Pd-S NCs show only 8.6% selectivity loss after the durability test in 0.05 M H_2SO_4 (Fig. S8 and Table S3 in the ESM).

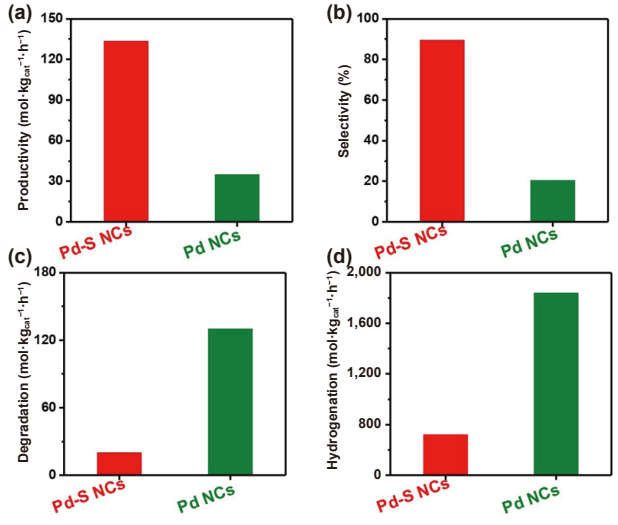

Figure 2 (a) H_2O_2 productivity, (b) selectivity, (c) degradation and (d) hydrogenation of different catalysts under optimal conditions. Reaction conditions: V_{CH3OH} = 7.0 mL, V_{H2O} = 3.0 mL, $H_2/O_2/Ar$ = 0.18/0.4/3.42 MPa, T = 0 °C, catalyst loading amount: 5 wt.%, catalyst weight: 5 mg, stirring: 800 rpm, and reaction time: 30 min.

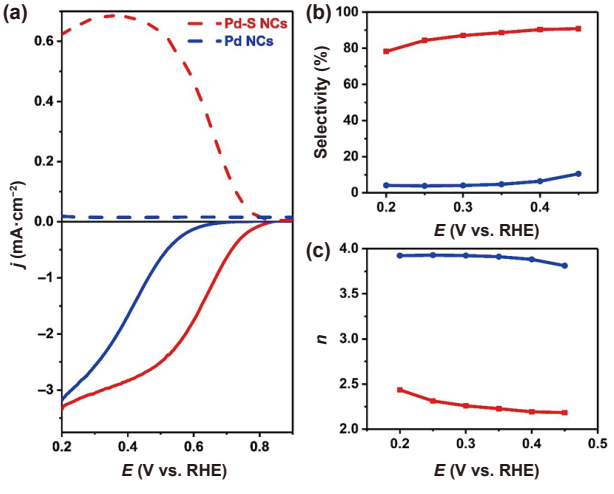

Figure 3 (a) RRDE voltammograms of the Pd NCs and Pd-S NCs at 1,600 rpm in O_2-saturated 0.05 M H_2SO_4 with the disk current density and ring current. The scan rate is 10 $mV \cdot s^{-1}$. Calculated (b) selectivity and (c) number of transferred electrons for the different catalysts at various potentials in a 0.05 M H_2SO_4 electrolyte. The colour scheme in (a) applies to (b) and (c).

Inspired by the excellent performance of Pd-S NCs for H_2O_2 production through DSHP and ORR, the production rate (36 μmoL·h^{-1}), which is about 7.2 and 4.5 times higher than those of TiO_2 and Pd NCs, respectively, indicating the photocatalytic H_2O_2 production can also be promoted by the distinct performance of Pd-S NCs for photocatalytic H_2O_2 production was also investigated. TiO_2 was selected as the support for both Pd-S NCs and Pd NCs. Figure S9 in the ESM shows the H_2O_2 production rate of different catalysts structure of Pd-S NCs with independent Pd sites.

To understand the underlying catalytic mechanisms of different catalysts, XPS analyses for Pd-S NCs and Pd NCs were performed. As can be seen from Fig. 4(a), two strong peaks located at 335.9 and 341.3 eV of Pd NCs corresponding to Pd^0 $3d_{5/2}$ and Pd^0 $3d_{3/2}$, respectively. Meanwhile, two weak shoulder peaks at 337.2 and 342.6 eV belong to Pd^{2+} $3d_{5/2}$ and Pd^{2+} $3d_{3/2}$, respectively. However, compared with Pd NCs, a slight shift of Pd^0 $3d_{5/2}$ peak toward the lower values (335.6 and 341.0 eV) is observed for Pd-S NCs, indicating some electron transfer from S to Pd. The surface valance band spectra of Pd NCs and Pd-S NCs were also tested by XPS. The modulated electronic effect further tunes the binding strength of O-related intermediates, which eventually modulates the catalytic activity. As can be seen from Fig. S10 in the ESM, compared with Pd NCs, introducing S to Pd can upshift the gravity of d-band center (Pd-S NCs), which is beneficial to strengthen the adsorption of O-related intermediates.

To figure out the influence of unique structure on catalytic performance, O_2 temperature-programmed desorption (O_2-TPD) measurements for PdS NCs and Pd NCs were performed. Both Pd-S NCs and Pd NCs show two peaks at 147.6 and 405.5 °C (Fig. 4(b)), which was attributed to the O_2 intermediate and Pd–O bond stretching mode, respectively. The other peak for Pd NCs was located at 301.2 °C, which was assigned to O^- intermediate. Compared with Pd NCs, the peak of O^- at Pd-S NCs was not found, indicating the isolated Pd sites can inhibit O–O dissociation, thus enhancing the selectivity of H_2O_2 synthesis. Moreover, diffuse reflectance infrared Fourier transform spectroscopy (DRIFTS) measurement was further employed to study the performance difference between Pd-S NCs and Pd NCs. Figure 4(c) shows the different CO adsorption patterns of Pd-S and Pd NCs in DRIFTS spectra, which can be ascribed to the linear CO species on isolated Pd sites (2,069 cm^{-1}) and bridged CO species on Pd facets (1,897 cm^{-1}), respectively [51, 52]. It has been accepted that inhibiting the dissociation of O–O bonds is crucial for H_2O_2 synthesis. Therefore, the isolated Pd sites are more favorable for H_2O_2 formation by inhibiting O–O dissociation (Fig. 4(d)).

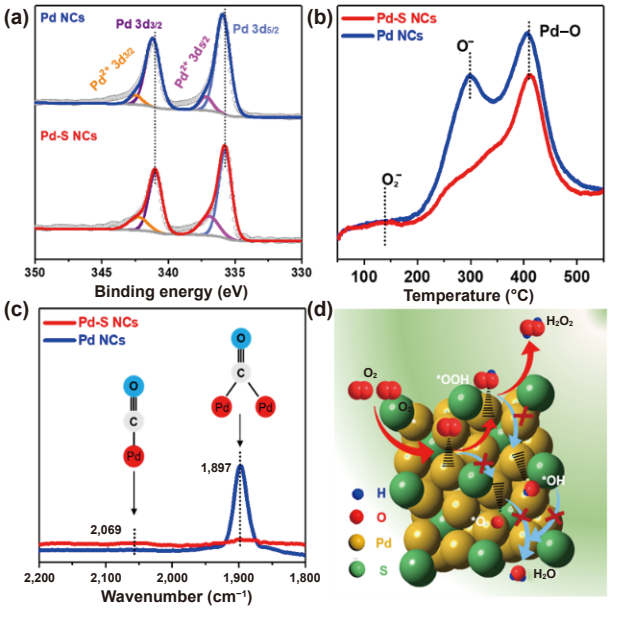

Figure 4 (a) XPS patterns of Pd 3d, (b) O_2-TPD profiles and (c) *in situ* DRIFTS of CO adsorption in Pd-S NCs and Pd NCs. (d) Schematic illustration of H_2O_2 formation on Pd-S NCs.

To further understand the high selectivity of Pd-S NCs for H_2O_2 production comparing to Pd NCs, we performed DFT calculations. The Pd (111) and S-terminated Pd_4S phase (110) surfaces are chosen for study in this part, because they are most stable in thermodynamics. As depicted in Fig. 5, we calculated the activation free energies required for O_2* and OOH* dissociation and associative hydrogenation on two surfaces. As shown in Fig. 5(a), in the case of Pd (111), we can find that the dissociation steps are more favored for both of O_2* and OOH* comparing to their respective associative hydrogenation steps. While for the Pd_4S (110) surface (Fig. 5(b)), it shows completely opposite results that the associative hydrogenation steps become much more preferred. It is consistent with the experimental measurements that the Pd-S NCs have high selectivity for H_2O_2, and the O_2 is inclined to be fully reduced on the surface of Pd NCs. To understand the significant difference between Pd (111) and Pd_4S phase (110) at the atomic level, we analyzed the structures of transition states for ORR. From Fig. 5 and Figs. S11–S13 in the ESM, we can find that the S atoms on Pd_4S phase (110) surface isolate the active sites of Pd, and a direct consequence is that the O* stays on the top site of Pd in the transition states of dissociation steps, which is energetically unfavorable. By contrast, the energies of transition states for the dissociation steps on Pd (111) can be lowered by the neighboring Pd atoms. Therefore, we can conclude that the difference in the atom composition and arrangement is the key factor for the different ORR mechanisms on the surfaces of Pd (111) and Pd_4S phase (110).

4 Conclusions

In summary, we have revealed that Pd-S NCs with atomically isolated Pd sites can be adopted as highly robust and versatile catalysts for the synthesis of H_2O_2 for the first time. In the DSHP, Pd-S NCs have achieved the excellent activity of 133.6 mol·kg$_{cat}^{-1}$·h^{-1} and selectivity (89.5%) and negligible H_2O_2 degradation. As the ORR electrocatalysts and photocatalytic catalysts, Pd-S NCs can also exhibit promising activity toward H_2O_2 production. Simultaneously, they have exhibited enough

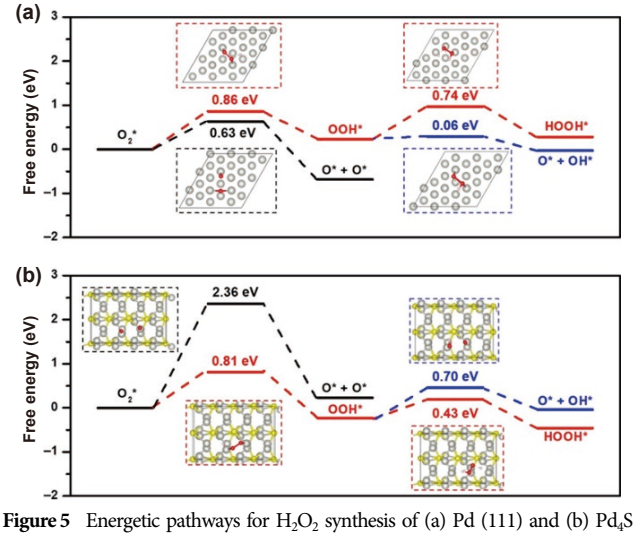

Figure 5 Energetic pathways for H_2O_2 synthesis of (a) Pd (111) and (b) Pd_4S (110).

capacity to maintain satisfactory stability with slight activity decay for the H_2O_2 production. Detailed mechanism investigation proved that the high electron density of Pd atom enhances the adsorption and activation of O_2, which is beneficial for improving H_2O_2 production rate. In addition, the presence of S in Pd-S NCs contributes to the formation of isolated Pd atoms, thus boosting the H_2O_2 selectivity and reducing its degradation. The present effort in this work demonstrates a new class of trifunctional Pd-based nanocatalysts with excellent performance for H_2O_2 synthesis and beyond.

Acknowledgements

This work was financially supported by the National Key R&D Program of China (Nos. 2017YFA0208200 and 2016YFA0204100), the National Natural Science Foundation of China (No. 22025108), the Priority Academic Program Development of Jiangsu Higher Education Institutions (PAPD), and the start-up supports from Xiamen University.

Electronic Supplementary Material: Supplementary material (SEM-EDS and TEM characterizations, electrochemical measurements, photocatalytic performance, DFT calculations, and comparison of catalytic performances for different catalysts) is available in the online version of this article at https://doi.org/10.1007/s12274-021-3786-0.

References

[1] Wilson, N. M.; Pan, Y. T.; Shao, Y. T.; Zuo, J. M.; Yang, H.; Flaherty, D. W. Direct synthesis of H_2O_2 on AgPt octahedra: The importance of Ag-Pt coordination for high H_2O_2 selectivity. *ACS Catal.* **2018**, *8*, 2880–2889.

[2] Salmerón, I.; Plakas, K. V.; Sirés, I.; Oller, I.; Maldonado, M. I.; Karabelas, A. J.; Malato, S. Optimization of electrocatalytic H_2O_2 production at pilot plant scale for solar-assisted water treatment. *Appl. Catal. B: Environ.* **2019**, *242*, 327–336.

[3] Verdaguer-Casadevall, A.; Deiana, D.; Karamad, M.; Siahrostami, S.; Malacrida, P.; Hansen, T. W.; Rossmeisl, J.; Chorkendorff, I.; Stephens, I. E. L. Trends in the electrochemical synthesis of H_2O_2: Enhancing activity and selectivity by electrocatalytic site engineering. *Nano Lett.* **2014**, *14*, 1603–1608.

[4] Ye, Z. H.; Guelfi, D. R. V.; Álvarez, G.; Alcaide, F.; Brillas, E.; Sirés, I. Enhanced electrocatalytic production of H_2O_2 at Co-based air-diffusion cathodes for the photoelectro-Fenton treatment of bronopol. *Appl. Catal. B: Environ.* **2019**, *247*, 191–199.

[5] De Faveri, G.; Ilyashenko, G.; Watkinson, M. Recent advances in catalytic asymmetric epoxidation using the environmentally benign oxidant hydrogen peroxide and its derivatives. *Chem. Soc. Rev.* **2011**, *40*, 1722–1760.

[6] Lane, B. S.; Burgess, K. Metal-catalyzed epoxidations of alkenes with hydrogen peroxide. *Chem. Rev.* **2003**, *103*, 2457–2474.

[7] Li, H. B.; Zheng, B.; Pan, Z. Y.; Zong, B. N.; Qiao, M. H. Advances in the slurry reactor technology of the anthraquinone process for H_2O_2 production. *Front. Chem. Sci. Eng.* **2018**, *12*, 124–131.

[8] Iqbal, W.; Qiu, B. C.; Zhu, Q. H.; Xing, M. Y.; Zhang, J. L. Self-modified breaking hydrogen bonds to highly crystalline graphitic carbon nitrides nanosheets for drastically enhanced hydrogen production. *Appl. Catal. B: Environ.* **2018**, *232*, 306–313.

[9] Campos-Martin, J. M.; Blanco-Brieva, G.; Fierro, J. L. G. Hydrogen peroxide synthesis: An outlook beyond the anthraquinone process. *Angew. Chem., Int. Ed.* **2006**, *45*, 6962–6984.

[10] Liu, Y. M.; Quan, X.; Fan, X. F.; Wang, H.; Chen, S. High-yield electrosynthesis of hydrogen peroxide from oxygen reduction by hierarchically porous carbon. *Angew. Chem., Int. Ed.* **2015**, *54*, 6837–6841.

[11] Guo, Y. Y.; Dai, C. N.; Lei, Z. G.; Chen, B. H.; Fang, X. C. Synthesis of hydrogen peroxide over Pd/SiO_2/COR monolith catalysts by anthraquinone method. *Catal. Today* **2016**, *276*, 36–45.

[12] Kanungo, S.; Paunovic, V.; Schouten, J. C.; D' Angelo, M. F. N. Facile synthesis of catalytic AuPd nanoparticles within capillary microreactors using polyelectrolyte multilayers for the direct synthesis of H_2O_2. *Nano Lett.* **2017**, *17*, 6481–6486.

[13] Melchionna, M.; Fornasiero, P.; Prato, M. The rise of hydrogen peroxide as the main product by metal-free catalysis in oxygen reductions. *Adv. Mater.* **2019**, *31*, 1802920.

[14] Yang, S.; Verdaguer-Casadevall, A., Arnarson, L.; Silvioli, L.; Čolić, V.; Frydendal, R.; Rossmeisl, J.; Chorkendorff, I.; Stephens, I. E. L. Toward the decentralized electrochemical production of H_2O_2: A focus on the catalysis. *ACS Catal.* **2018**, *8*, 4064–4081.

[15] Dong, K.; Lei, Y.; Zhao, H. T.; Liang, J.; Ding, P.; Liu, Q.; Xu, Z. Q.; Lu, S. Y.; Li, Q.; Sun, X. P. Noble-metal-free electrocatalysts toward H_2O_2 production. *J. Mater. Chem. A* **2020**, *8*, 23123–23141.

[16] Wang, Z.; Li, Q. K.; Zhang, C. H.; Cheng, Z. H.; Chen, W. Y.; Mchugh, E. A.; Carter, R. A.; Yakobson, B. I.; Tour, J. M. Hydrogen peroxide generation with 100% faradaic efficiency on metal-free carbon black. *ACS Catal.* **2021**, *11*, 2454–2459.

[17] Wilson, N. M.; Flaherty, D. W. Mechanism for the direct synthesis of H_2O_2 on Pd clusters: Heterolytic reaction pathways at the liquid-solid interface. *J. Am. Chem. Soc.* **2016**, *138*, 574–586.

[18] Lari, G. M.; Puértolas, B.; Shahrokhi, M.; López, N.; Pérez-Ramírez, J. Hybrid palladium nanoparticles for direct hydrogen peroxide synthesis: The key role of the ligand. *Angew. Chem., Int. Ed.* **2017**, *56*, 1775–1779.

[19] Vu, H. T. T.; Vo, V. L. N.; Chung, Y. M. Geometric, electronic, and synergistic effect in the sulfonated carbon-supported Pd catalysts for the direct synthesis of hydrogen peroxide. *Appl. Catal. A: Gen.* **2020**, *607*, 117867.

[20] Jin, Z.; Liu, Y. F.; Wang, L.; Wang, C. T.; Wu, Z. Y.; Zhu, Q. Y.; Wang, L. X.; Xiao, F. S. Direct synthesis of pure aqueous H_2O_2 solution within aluminosilicate zeolite crystals. *ACS Catal.* **2021**, *11*, 1946–1951.

[21] Han, G. H.; Lee, S. H.; Hwang, S. Y.; Lee, K. Y. Advanced development strategy of nano catalyst and DFT calculations for direct synthesis of hydrogen peroxide. *Adv. Energy Mater.* **2021**, 2003121.

[22] Jiang, Y. Y.; Ni, P. J.; Chen, C. X.; Lu, Y. Z.; Yang, P.; Kong, B.; Fisher, A.; Wang, X. Selective electrochemical H_2O_2 production through two-electron oxygen electrochemistry. *Adv. Energy Mater.* **2018**, *8*, 1801909.

[23] Zheng, L. H.; Su, H. R.; Zhang, J. Z.; Walekar, L. S.; Molamahmood, H. V.; Zhou, B. X.; Long, M. C.; Hu, Y. H. Highly selective photocatalytic production of H_2O_2 on sulfur and nitrogen co-doped graphene quantum dots tuned TiO_2. *Appl. Catal. B: Environ.* **2018**, *239*, 475–484.

[24] Kim, J. S.; Kim, H. K.; Kim, S. H.; Kim, I.; Yu, T.; Han, G. H.; Lee, K. Y.; Lee, J. C.; Ahn, J. P. Catalytically active Au layers grown on Pd nanoparticles for direct synthesis of H_2O_2: Lattice strain and charge-transfer perspective analyses. *ACS Nano* **2019**, *13*, 4761–4770.

[25] Lee, J. H.; Cho, H.; Park, S. O.; Hwang, J. M.; Hong, Y. R. N.; Sharma, P.; Jeon, W. C.; Cho, Y.; Yang, C.; Kwak, S. K. et al. High performance H_2O_2 production achieved by sulfur-doped carbon on CdS photocatalyst via inhibiting reverse H_2O_2 decomposition. *Appl. Catal. B: Environ.* **2021**, *284*, 119690.

[26] Zhao, Y. J.; Liu, Y.; Wang, Z. Z.; Ma, Y. R.; Zhou, Y. J.; Shi, X. F.; Wu, Q. Y.; Wang, X.; Shao, M. W.; Huang, H. et al. Carbon nitride assisted 2D conductive metal-organic frameworks composite photocatalyst for efficient visible light-driven H_2O_2 production. *Appl. Catal. B: Environ.* **2021**, *289*, 120035.

[27] Wu, S.; Yu, H. T.; Chen, S.; Quan, X. Enhanced photocatalytic H_2O_2 production over carbon nitride by doping and defect engineering. *ACS Catal.* **2020**, *10*, 14380–14389.

[28] Chen, S. C.; Chen, Z. H.; Siahrostami, S.; Higgins, D.; Nordlund, D.; Sokaras, D.; Kim, T. R.; Liu, Y. Z.; Yan, X. Z.; Nilsson, E. et al. Designing boron nitride islands in carbon materials for efficient electrochemical synthesis of hydrogen peroxide. *J. Am. Chem. Soc.* **2018**, *140*, 7851–7859.

[29] Burek, B. O.; Bahnemann, D. W.; Bloh, J. Z. Modeling and optimization of the photocatalytic reduction of molecular oxygen to hydrogen peroxide over titanium dioxide. *ACS Catal.* **2019**, *9*, 25–37.

[30] Wang, F.; Xia, C. G.; de Visser, S. P.; Wang, Y. How does the oxidation state of palladium surfaces affect the reactivity and selectivity of direct synthesis of hydrogen peroxide from hydrogen and oxygen gases? A density functional study. *J. Am. Chem. Soc.* **2019**, *141*, 901–910.

[31] Deschner, B. J.; Doronkin, D. E.; Sheppard, T. L.; Zimina, A.; Grunwaldt, J. D.; Dittmeyer, R. Effect of selectivity enhancers on the structure of palladium during high-pressure continuous-flow direct synthesis of hydrogen peroxide in ethanol. *J. Phys. Chem. C* **2021**, *125*, 3451–3462.

[32] Cai, H. Z.; Chen, B. B.; Zhang, X.; Deng, Y. C.; Xiao, D. Q.; Ma, D.; Shi, C. Highly active sites of low spin $Fe_{II}N_4$ species: The identification and the ORR performance. *Nano Res.* **2021**, *14*, 122–130.

[33] Ding, R.; Liu, Y. D.; Rui, Z. Y.; Li, J.; Liu, J. G.; Zou, Z. G. Facile grafting strategy synthesis of single-atom electrocatalyst with enhanced ORR performance. *Nano Res.* **2020**, *13*, 1519–1526.

[34] Lu, Y. Z.; Wang, J.; Peng, Y. C.; Fisher, A.; Wang, X. Highly efficient and durable Pd hydride nanocubes embedded in 2D amorphous NiB nanosheets for oxygen reduction reaction. *Adv. Energy Mater.* **2017**, *7*, 1700919.

[35] Bu, L. Z.; Feng, Y. G.; Yao, J. L.; Guo, S. J.; Guo, J.; Huang, X. Q. Facet and dimensionality control of Pt nanostructures for efficient oxygen reduction and methanol oxidation electrocatalysts. *Nano Res.* **2016**, *9*, 2811–2821.

[36] Zhou, R. F.; Zheng, Y.; Jaroniec, M.; Qiao, S. Z. Determination of the electron transfer number for the oxygen reduction reaction: From theory to experiment. *ACS Catal.* **2016**, *6*, 4720–4728.

[37] Freakley, S. J.; He, Q.; Harrhy, J. H.; Lu, L.; Crole, D. A.; Morgan, D. J.; Ntainjua, E. N.; Edwards, J. K.; Carley, A. F.; Borisevich, A. Y. et al. Palladium-tin catalysts for the direct synthesis of H_2O_2 with high selectivity. *Science* **2016**, *351*, 965–968.

[38] Xu, H. X.; Cheng, D. J.; Gao, Y.; Zeng, X. C. Assessment of catalytic activities of gold nanoclusters with simple structure descriptors. *ACS Catal.* **2018**, *8*, 9702–9710.

[39] Yi, Y. H.; Xu, C.; Wang, L.; Yu, J.; Zhu, Q. R.; Sun, S. Q.; Tu, X.; Meng, C. G.; Zhang, J. L.; Guo, H. C. Selectivity control of H_2/O_2 plasma reaction for direct synthesis of high purity H_2O_2 with desired concentration. *Chem. Eng. J.* **2017**, *313*, 37–46.

[40] Gong, X. X.; Lewis, R. J.; Zhou, S.; Morgan, D. J.; Davies, T. E.; Liu, X.; Kiely, C. J.; Zong, B. N.; Hutchings, G. J. Enhanced catalyst selectivity in the direct synthesis of H_2O_2 through Pt incorporation into TiO_2 supported AuPd catalysts. *Catal. Sci. Technol.* **2020**, *10*, 4635–4644.

[41] Tsukamoto, D.; Shiro, A.; Shiraishi, Y.; Sugano, Y.; Ichikawa, S.; Tanaka, S.; Hirai, T. Photocatalytic H_2O_2 production from ethanol/O_2 system using TiO_2 loaded with Au-Ag bimetallic alloy nanoparticles. *ACS Catal.* **2012**, *2*, 599–603.

[42] Choi, C. H.; Kim, M.; Kwon, H. C.; Cho, S. J.; Yun, S.; Kim, H. T.; Mayrhofer, K. J. J.; Kim, H.; Choi, M. Tuning selectivity of electrochemical reactions by atomically dispersed platinum catalyst. *Nat. Commun.* **2016**, *7*, 10922.

[43] Yang, S.; Kim, J.; Tak, Y. J.; Soon, A.; Lee, H. Single-atom catalyst of platinum supported on titanium nitride for selective electrochemical reactions. *Angew. Chem., Int. Ed.* **2016**, *55*, 2058–2062.

[44] Shen, R. A.; Chen, W. X.; Peng, Q.; Lu, S. Q.; Zheng, L. R.; Cao, X.; Wang, Y.; Zhu, W.; Zhang, J. T.; Zhuang, Z. B. et al. High-concentration single atomic Pt sites on hollow CuSx for selective O_2 reduction to H_2O_2 in acid solution. *Chem* **2019**, *5*, 2099–2110.

[45] Feng, Y. G.; Yang, C. Y.; Fang, W.; Huang, B. L.; Shao, Q.; Huang, X. Q. Antipoisonedoxygen reduction by the interface modulated Pd@NiO core@shell. *Nano Energy* **2019**, *58*, 234–243.

[46] Zhang, J.; Qiao, M.; Li, Y. F.; Shao, Q.; Huang, X. Q. Highly active and selective electrocatalytic CO_2 conversion enabled by core/shell Ag/(amorphous-Sn(IV)) nanostructures with tunable shell thickness. *ACS Appl. Mater. Interfaces* **2019**, *11*, 39722–39727.

[47] Zhang, J. B.; Xu, W. W.; Xu, L.; Shao, Q.; Huang, X. Q. Concavity tuning of intermetallic Pd-Pb nanocubes for selective semihydrogenation catalysis. *Chem. Mater.* **2018**, *30*, 6338–6345.

[48] Cao, K. L.; Yang, H.; Bai, S. X.; Xu, Y.; Yang, C. Y.; Wu, Y.; Xie, M.; Cheng, T.; Shao, Q.; Huang, X. Q. Efficient direct H_2O_2 synthesis enabled by PdPb nanorings via inhibiting the O−O bond cleavage in O_2 and H_2O_2. *ACS Catal.* **2021**, *11*, 1106–1118.

[49] Xu, Y.; Bian, W. Y.; Pan, Q.; Chu, M. Y.; Cao, M. H.; Li, Y. Y.; Gong, Z. M.; Wang, R.; Cui, Y.; Lin, H. P. et al. Revealing the active sites of Pd nanocrystals for propyne semihydrogenation: From theory to experiment. *ACS Catal.* **2019**, *9*, 8471–8480.

[50] Zeng, Y. Q.; Wang, T. X.; Zhang, S. L.; Wang, Y. N.; Zhong, Q. Sol-gel synthesis of CuO-TiO_2 catalyst with high dispersion CuO species for selective catalytic oxidation of NO. *Appl. Surf. Sci.* **2017**, *411*, 227–234.

[51] Wang, S. L.; Gao, K. G.; Li, W.; Zhang, J. L. Effect of Zn addition on the direct synthesis of hydrogen peroxide over supported palladium catalysts. *Appl. Catal. A: Gen.* **2017**, *531*, 89–95.

[52] Gao, F.; Wang, L. Y.; Goodman, D. W. CO oxidation over AuPd(100) from ultrahigh vacuum to near-atmospheric pressures: The critical role of contiguous Pd atoms. *J. Am. Chem. Soc.* **2009**, *131*, 5734–5735.